

Plasmonic brownian ratchets for directed transport of analytes

Marciano Palma do Carmo,^{*,†} David Mack,[‡] Diane J. Roth,[†] Miao Zhao,[†] Ancin M. Devis,[†] Francisco J. Rodríguez-Fortuño,[†] Stefan A. Maier,^{¶,‡} Paloma A. Huidobro,^{§,||,⊥} and Aliaksandra Rakovich^{*,†}

[†]*Physics Department, King's College London, London, UK*

[‡]*Department of Physics, Imperial College London, London, UK*

[¶]*School of Physics and Astronomy, Monash University, Clayton Victoria, Australia*

[§]*Departamento de Física Teórica de la Materia Condensada, Universidad Autónoma de Madrid, Spain*

^{||}*Condensed Matter Physics Center (IFIMAC), Universidad Autónoma de Madrid, Madrid, Spain*

[⊥]*Instituto de Telecomunicações, Instituto Superior Tecnico - University of Lisbon, Lisboa, Portugal*

E-mail: marciano.palma_do_carmo@kcl.ac.uk; aliaksandra.rakovic@kcl.ac.uk

Abstract

Controlled long-range transport of micro- and nano-scale objects is a key requirement in lab-on-a-chip and microfluidic applications, enabling the efficient capture, concentration, manipulation, and detection of analytes. Traditional methods such as microfluidic pumps and optical trapping face challenges including high power consumption and limited range of action. This study introduces a plasmonic Brownian ratchet designed for the directed transport of dielectric nanometer-sized particles at low

optical powers. Through numerical simulations, the ratchet geometry was optimized to enhance electric fields, optical forces, and trapping potentials. Experimentally, the plasmonic ratchet demonstrated the ability to rectify random thermal motion of 40 nm polystyrene spheres over extended distances in a specific direction, achieving velocities up to 2.4 $\mu\text{m/s}$ at excitation powers as low as 0.785 kW/cm^2 . This plasmonic ratchet offers a robust and efficient solution for the targeted delivery and concentration of nanoscale analytes on chips, with significant implications for advancing applications in the life sciences.

Introduction

Controlled long-range transport of micro/nano-scale objects is a common prerequisite in lab-on-a-chip and microfluidic applications, where it enables efficient capture, concentration, manipulation and detection of analytes, for purposes ranging from moving and sorting of different types of organisms, such as bacteria, microalgae and blood cells,¹ to stretching and bending of DNA and RNA,² to investigations of forces exerted by molecular motors, chromosome sorting,^{3,4} classification of cancer cells⁵ and disease diagnostics.⁶ Various methods can be employed to achieve transport of micro- to nano-scale particles, the most common of which include the use of microfluidic pumps,^{7,8} optical trapping and manipulation of nanoparticles,⁹ the use of capillary forces,^{10,11} and the diffusion of particles due to Brownian motion.¹⁰ Whilst each of these methods offers its own distinct advantages, each also presents its own set of challenges. The use of microfluidic pumps,^{7,8} for example, often requires the use of high flow rates, resulting in significant consumption of power and relatively short periods of time spent by the analytes in the sensing areas. The use of optical forces does provide a superior level of control over the trapping and manipulation of nanoscale objects; however, it is extremely limited in its range of action (to the order of the diffraction limit^{9,12}) and is also subject to requirements for the optical potential to be deeper than the thermal energy of the system (*i.e.* that $|\Delta U| > k_B T$), necessitating high optical powers that are

detrimental for biological analytes such as cells or viruses. Finally, the use of capillary forces and Brownian diffusion^{10,11} to transport the analytes do circumvent the issue of high power consumption; however, both are still subject to limitations imposed by the passive flow of analytes through the sensing areas and are therefore reliant on high sample concentrations.

Nonetheless, the transport of analytes by Brownian motion is extremely appealing because such transport can take place over very long distances and at very low power cost, without a necessity for complex fluidic systems and external flows. The main drawback of the technique - the lack of directionality of the analyte motion - can be overcome by an application of an asymmetric and periodic external potential, that drives the system out of equilibrium and endues a preferential direction to the Brownian motion of analytes. More specifically, the working principle of a Brownian Ratchet involves the periodic trapping of the analytes by the asymmetric potential and the free diffusion of the analytes between the periods of trapping, as depicted schematically in Figure 1. The potential applied is not limited in its nature, and so mechanical,¹¹ electrical,^{13,14} thermal,¹⁵⁻¹⁸ and photonic¹⁹ ratchets have been previously reported. In all cases, the key requirements for rectification of Brownian motion to occur is that the potential (ΔU) remains sufficiently deep to trap the analytes and that the time that said potential remain off (τ_{off}) lies between the two limits corresponding to the time it takes for analyte particles to diffuse forward (τ_F) and backwards (τ_B) to the adjacent potential unit cells from the position of the potential minima, *i.e.* distances r and $L-r$ in Figure 1, where L is the ratchet period and r is the shortest distance from the potential minimum to the next unit cell. For a 2-dimensional ratchet, with a repeating structure along two different directions and particles diffusing above it, these respective times can be calculated using the diffusion theory:

$$\tau_F = \frac{r^2}{2D} \quad \text{and} \quad \tau_B = \frac{(L-r)^2}{2D}, \quad (1)$$

where D is the diffusion constant of the analyte particles in solution. Using these defini-

tions, the requirement for rectification of Brownian motion by the ratchet can be stated mathematically as:

$$\tau_B > \tau_{off} > \tau_F \tag{2}$$

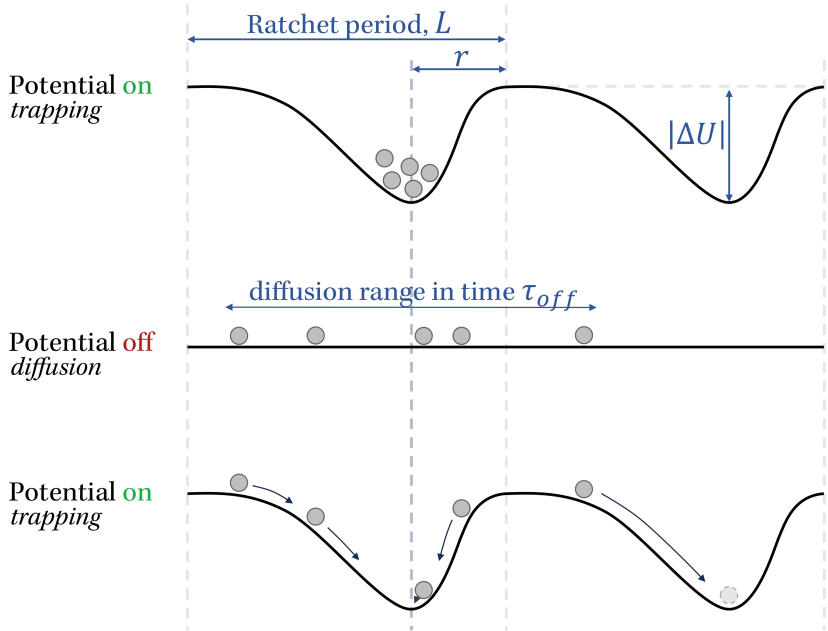


Figure 1: The working principles of a Brownian ratchet. During the times that the trapping potential remains on, τ_{on} , the analyte particles are driven towards locations corresponding to potential minima and remain trapped there. When the potential is then turned off, for a period of τ_{off} , the particles are able to diffuse freely in any direction with a characteristic diffusion coefficient, D . Once the potential is turned on again, the particles are re-trapped and driven towards potential minima again. For rectification of Brownian motion to occur, the time that the potential remains off must be larger than the average time it takes for an analyte particle to diffuse towards the next potential well (distance r in the figure) but smaller than the time it would take it to diffuse to the previous potential (i.e. distance $L-r$).

Whilst the requirements described above are general to all types of Brownian ratchets, the nature of the analyte particles often dictates the optimum type of potential to be applied. For instance, the size of the particles being transported and their diffusion constant affect their interaction with the potential landscape, their ability to overcome energy barriers and the timescale of the particle transport. For example, for extremely small analytes such as viral particles (typically sub-200 nm in size), mechanical ratchets would generally be considered non-ideal due to their sensitivity to environmental conditions (e.g. temperature

and viscosity), limited throughput (processing of a few particles at a time) and potential mechanical damage to the particles.^{20,21} On the other hand, electrical and photonic ratchets, whilst offering higher throughput and reduced potential damage, are both characterized by relatively large power consumption.^{15,22} In the case of the latter, however, plasmonics has been proposed as means of remedying this issue.²³

Plasmonic nanostructures exhibit localized surface plasmon resonances (LSPRs), which strongly concentrate electric fields in their near-fields,^{24,25} resulting in a drastic reduction of powers needed to operate the plasmonic ratchet when compared to their photonic counterparts. Additionally, the geometry and dimensions of plasmonic structures can be easily tailored for specific types of analyte particles and types, offering scalability of the overall system. Whilst plasmonic ratchets have been theorized,²³ as yet no reports of their experimental verification have been published and it is this oversight that current work aims to correct. To achieve this, we design, fabricate and test an array of plasmonic structures capable of generating asymmetric potential landscape for the ratchetting of viral particles. We do so by employing dielectric nanoparticles of sizes and polarizabilities similar to those of typical viral particles as the model system in our investigations, and show that such particles can be successfully transported over long distances using the developed plasmonic ratchet under chopped optical excitation.

Results and discussion

Optimization of plasmonic ratchet design

For plasmonic ratchet to operate efficiently, the key requirements are to provide an asymmetric trapping potential for any analytes located above it and that the depth of this potential is larger than the thermal energy of the system. As such, the asymmetry and the depth of the potential were used as key figures of merit when designing and optimizing our plasmonic ratchet structure. During this process, both parameters were obtained by first using

numerical simulations (COMSOL Multiphysics) to evaluate the electric field enhancement produced by the proposed plasmonic structure upon plane wave illumination and then using the dipolar approximation to calculate the electric potential along the central gap of and above the plasmonic structure (as shown in Figure S2 of the SI document). This direction was considered as the dimer antennas offer greatest electric field enhancements in their gaps, thereby providing the deepest trapping potentials in these locations. Several designs were considered (work not presented here), but the design consisting of three sets of rectangular gap-antennas (as in Figure 2(a)), similar to that considered theoretically by Huidobro *et al.*,²³ was deemed to be the most promising. In this design, the changing lengths of the gap-antennas ensure a varying degree of coupling between the incident plane wave radiation and the antenna, resulting in a gradually decreasing electric field enhancements along the central gap of the ratchet unit cell. In turn, the varying field enhancements ensure the asymmetric trapping of the analyte particles, which is a pre-requisite for driving the system from equilibrium to rectify the Brownian motion of the particles.

Choosing this design as the basis, the geometrical parameters of the plasmonic ratchet structure were further optimised for rectification of Brownian motion of sub-200 nm particles, under 980 nm chopped excitation. Prior to considering the full ratchet structure, a single row of gap-antennas of Au material was optimized to resonate strongly at the target excitation wavelength of 980 nm, as measured by numerically-simulated optical cross-sections of the antenna in water. The width, height, length and gap of the rods were varied systematically until a broad resonance centred at 980 nm wavelength was obtained. The optimized structure was determined to consist of two rectangular rods, which were 125 nm in length, 50 nm in width and 50 nm in height (a 5 nm Cr adhesion layer and 45 nm Au layer).

Optimization studies were then extended to the full ratchet unit design shown in Figure 1(a), starting with all rods having the same length and same separations ($g = 30$ nm), and then adjusting the asymmetry of the structure by shortening the rods in each successive row of gap-antennas. Adjustments to rod lengths were made according to the angle that

the line joining the corners of the rods made with the symmetry axis of the structure, as illustrated by red dashed lines in Figure 2(a). The angle of 9° resulted in the strongest and spatially most extended electric field enhancements (see section 1.1 of SI for full details).

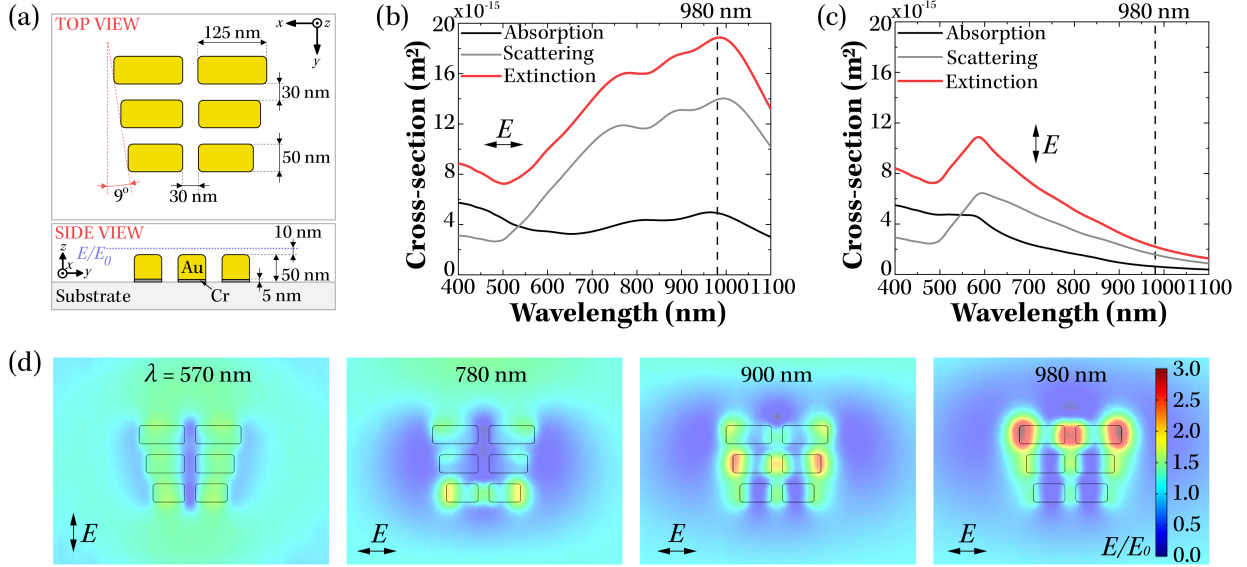


Figure 2: Numerical calculations of the optical response of plasmonic ratchets. **(a)** Optimised structure of the plasmonic ratchet, shown in top view (top box) and in side view (bottom box). The blue dashed line denotes the plane for which the electric field enhancement maps in (d) were calculated. The system of axes shown in panel (a) is maintained throughout the text. **(b)** and **(c)** show the numerically simulated absorption (black line), scattering (grey line) and extinction (red line) cross-sections for the ratchet in water, when excited with plane waves of two orthogonal polarisations. The polarisation of electric field is indicated using black arrows in each panel. The black dashed lines in (b) and (c) represent the wavelength of excitation used in ratchetting experiments ($\lambda_{exc} = 980 \text{ nm}$). **(d)** The calculated electric field enhancements at a plane located $z = 10 \text{ nm}$ above the top of plasmonic ratchets, for different wavelengths of excitations and different polarisations of incident electric field, as indicated in each plot.

Figure 2 shows the calculated cross-sections (panels (b) and (c)) of the designed plasmonic structures and the electric field enhancements generated by them at different excitation wavelengths, and at a height of 10 nm above their top surface (panel (d)). For longitudinal polarization of the electric field (panel (b)), the cross-sections clearly display signatures of individual resonances of the three sets of gap-antennas that constitute the structure (at 780, 900 and 980 nm, respectively), with the highest peak at 980 nm corresponding to the longi-

tudinal mode of the longest gap-antenna of the set. All these signatures are absent from the cross-sections obtained for the transverse electric field polarization (panel (c)), displaying only a single peak at 570 nm that corresponds to the transverse mode of all the rods in the ratchet structure. The electric field profiles shown in Figure (d) confirm these observations - excitation of the antennas longitudinally at 780, 900 and 980 nm clearly triggers the longitudinal modes of the shortest, middle-length and longest antennas, respectively, whereas transverse excitation at 570 nm has no such preferential effect. Importantly, excitation of the ratchet with a 980 nm wavelength plane wave of longitudinal polarization produces continuous and strongly enhanced electric field above the ratchet surface ($E_{max}/E_0 = 3.01$), suggesting that strong, asymmetric and deep potentials should also be offered by such structures.

Having optimized the unit cell of our ratchet to generate strongest field enhancements above its surface, we then proceed to optimize the periodicity of the structure in both x and y directions, corresponding to longitudinal and transverse directions of the electric field respectively. To do so, we switched from dipolar approximation to using the full Maxwell Stress Tensor (MST) calculation method, detailed in the methods section, to account for the effect that the polarization of the analyte particle has on the electric fields in its vicinity. Here, simulations were performed using polystyrene (PS) spheres as a model system for viral particles, due to their comparable refractive indices and sizes.^{26,27}

By systematically varying the size of the ratchet unit cell in both x and y directions, whilst applying periodic boundary conditions, periodicities of 700 nm and 800 nm, respectively, were determined to be optimum for the generation of strongest optical forces (details of these investigations are provided in SI). Figure 3 shows the numerically-simulated results for 40 nm PS spheres located 80 nm above the ratchet. Panel (c) shows that, under 980 nm illumination of $1 \text{ mW } \mu\text{m}^{-2}$ intensity, the ratchet produces an asymmetric electric field profile that extends from the longest set of gap-antennas to the shortest ones. The asymmetry of the electric field profile results in generation of optical forces, that are shown in panel (a)

of the Figure 3. Here, it is clear the PS spheres are expected to be optically driven towards the ratchet structure and along its length: the z -component of the optical forces drives the particles towards the surface of the ratchet structures; the y -component acts to drive the particles towards the longest set of gap-antennas, reversing its sign as the position of the particle passes said location; and the x component of the optical force is always negligible, in reflection of the symmetry of the structure in this direction (Figure 3(c)).

The electric potential experienced by the 40 nm PS spheres, as they move above and along the ratchet unit, was obtained *via* integration of the optical forces (see SI for details of these calculations) and is shown in panel (b) of Figure 3. Critically, the depth of the potential is larger than the thermal energy of the system ($|\Delta U| \simeq 3.4 k_b T$), suggesting that designed structures are capable of efficiently trapping the PS spheres. Furthermore, the potential is clearly asymmetric, with the minimum off-set from the geometric centre of the ratchet unit cell ($y \simeq 65$ nm), allowing for the rectification of Brownian motion of PS spheres, as discussed previously. The minimum distance that PS spheres need to diffuse during the time period when the potential remains off is given by the y separation of the minimum and the maximum of the electric potential data, which was determined to be equal to $r = 318$ nm. Given that the unit cell length, L , of the designed ratchet is 700 nm, this corresponded to the maximum diffusion distance of $L - r = 382$ nm during the same period, for rectification of Brownian motion to occur. Using Equation 1, these distances can be converted into the limits for the time that the potential must remain off for the rectification to occur in water and at room temperature, to yield values of 4.6 and 6.7 ms for τ_F and τ_B respectively. Here, the Stokes' law diffusion coefficient was used,

$$D = \frac{k_b T}{6\pi\eta R_h} \quad (3)$$

where $\eta = 10^{-3}$ Pa s $^{-1}$ is the viscosity of water at room temperature ($T = 298$ K) and R_h is the hydrodynamic radius of the PS spheres, taken to be approximately equal to half of their

diameter (~ 20 nm).

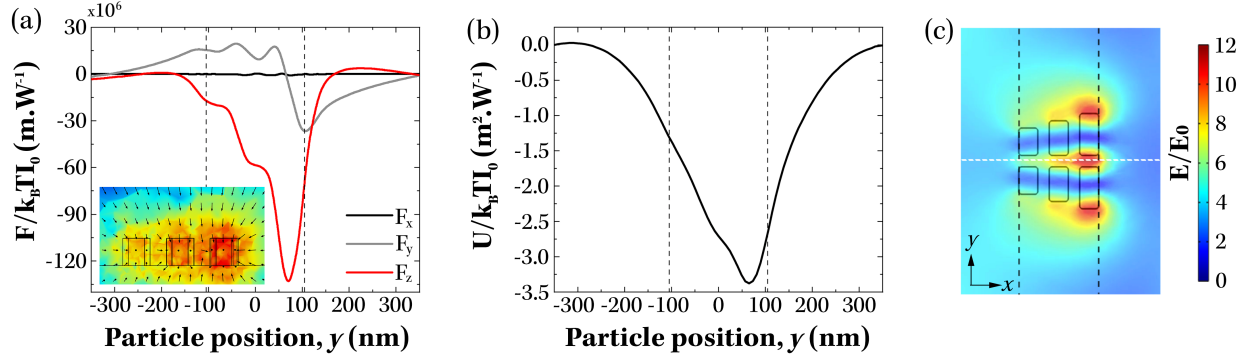


Figure 3: Numerical simulations of trapping ability of plasmonic ratchets. The calculated (a) optical forces and (b) the trapping potentials for a 40 nm PS nanoparticle located at a distance of $z = 80$ nm above the array of brownian ratchets, as a function of position y along the ratchet. The inset of panel (a) shows the stress tensor calculated for $x = 0$ plane. (c) Shows the electric field enhancement at $z = 80$ nm plane above the ratchet and the definition of x and y directions relative to the orientation of the ratchet. Results shown in panels (a) and (b) were calculated along the dashed white line in this map (corresponds to $x = 0$ nm and $z = 80$ nm direction). The black dashed lines in all panels represent the edges of the plasmonic ratchets along the y -direction.

Fabrication and characterization of the plasmonic ratchet

Plasmonic ratchets of optimized geometry were fabricated using standard ebeam lithography methods, as described in the methods section. An SEM image of some of the nanostructures of the fabricated periodic ratchet array is shown in Figure 4(a). The geometry of the ratchet unit cell was close to the target optimal values: the length of the longest rods was 121 ± 5 nm, the central gap was 32.7 ± 3.9 nm and the asymmetry angle θ was determined to be equal to $12.3^\circ \pm 1.6^\circ$. The width of the individual rods of 41.3 ± 2.5 nm was slightly smaller than the target value of 50 nm and resulted in slightly larger gaps between the rows of the gap-antennas (39.8 ± 2.5 nm instead of the target 30 nm). Nonetheless, the structures were clearly asymmetric and of comparable dimensions to the numerically optimized structures; thus, they were expected to perform well as a source of an asymmetric potential for the diffusion of PS spheres.

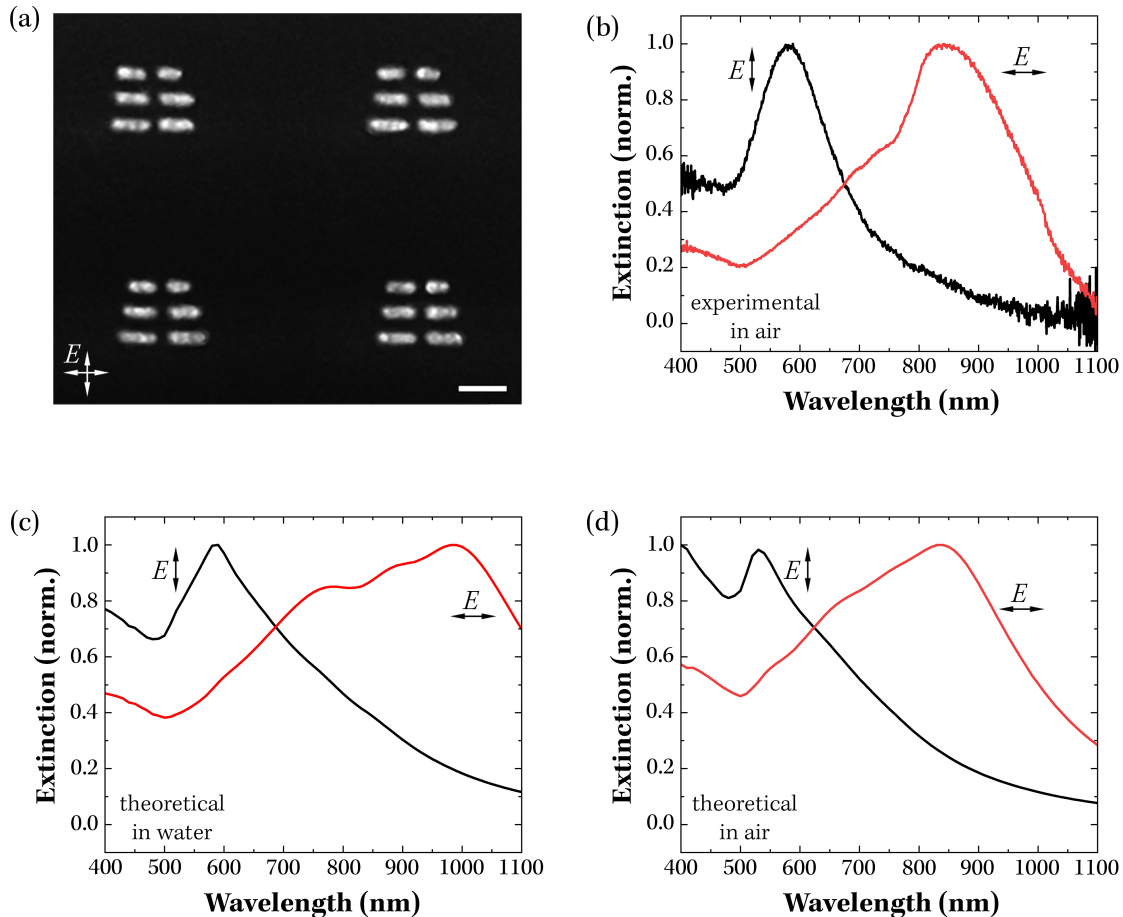


Figure 4: Fabrication and optical characterization of plasmonic ratchets. **(a)** Scanning electron microscope (SEM) image of the fabricated ratchet array. The scale bar in the image corresponds to 150 nm. **(b)** Experimental normalized extinction cross-sections measured for the plasmonic ratchet array in air. **(c)** and **(d)** show the numerically simulated and normalized extinction cross-sections of the ratchet array in water and in air, respectively.

To confirm that the fabricated ratchet could be driven by 980 nm excitation, the extinction spectrum of the plasmonic array was measured, at normal incidence and in air. As shown in Figure 4(b), the results of these measurements showed very good agreement with the numerically simulated optical response of the ratchets under similar excitation conditions (Figure 4(b)): both sets of data had characteristic peaks at ~ 850 nm and ~ 550 nm, corresponding to the longitudinal and transverse resonances of the longest gap-antennas in the structure, respectively, when in air. Equivalent numerical calculations performed for the ratchets immersed in water, results of which are shown in Figure 4(c), predict a red-shift of

these resonances and so confirm the expectation of a strong optical response of the fabricated structures at 980 nm excitation in water.

Experimental verification of plasmonic ratcheting

The motion of PS spheres above the fabricated plasmonic ratchets was recorded using a set-up shown in Figure 5(a). Briefly, the sample was mounted onto the microscope sample holder, and a drop of PS spheres suspension was placed on top. The sample was illuminated from the side with white-light, to enable dark-field imaging of the PS spheres by recording of the scattered light through an objective placed below the sample with an sCMOS camera. The excitation of the plasmonic ratchet was performed using 980 nm CW laser, incident directly downwards onto the sample, which could be blocked, run continuously or chopped, to allow recording of the Brownian diffusion, the trapping motion or the ratchetting motion of the PS spheres respectively. The recorded videos were analysed (as described in the experimental section), with the PS spheres identified and then traced through each frame of the video, yielding a set of trajectories for different PS spheres as a function of time. The corresponding set of displacement trajectories could then be obtained by subtracting each particle's initial position.

A subset of trajectories recorded for 40 nm PS spheres in water is shown in Figure 5(d), for Brownian, trapping and ratchetting motion respectively. As can be seen in this figure, for Brownian and trapping motion, the displacement trajectories show no preferential direction, and the average displacement of the particles undergoing Brownian motion is significantly larger than of those that are trapped by the ratchets. Conversely, particles undergoing ratchetting have a strong preferential direction, displacing primarily along a single direction (an angle of 90° in Figure 5(d), corresponding to x axis in Figures 2 and 3). For all types of motion, the displacement trajectories could be further statistically analysed, to yield sets of data of the mean displacement of all detected particles along the x and y direction as a function of time, as shown in panels (b) and (c) of Figure 5 for Brownian and ratchetting

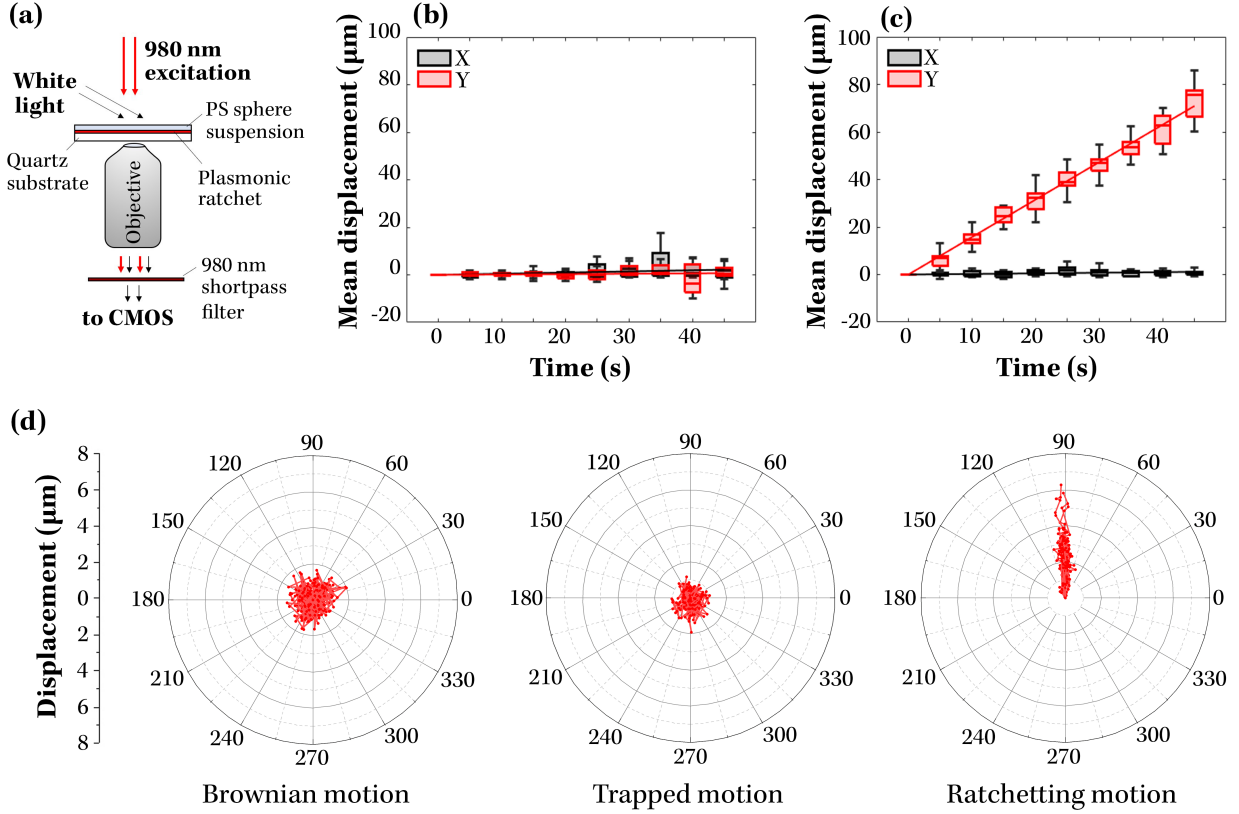


Figure 5: Motion of 40 nm PS spheres under different illumination conditions. Panel (a) shows the set-up used for recording the motion of PS spheres above the plasmonic ratchets. Panels (b) and (c) compare the average x and y displacements of PS particles undergoing Brownian motion and ratchetting, respectively, as a function of motion time. Panel (c) shows, left-to-right, traces of 10 to 20 PS particles undergoing Brownian, trapping or ratchetting motion over a time period of 270 ms. Traces are shown in polar coordinates and are all relative, *i.e.* they are measured relative to the position of each particle when first detected.

motion respectively. From these, the average velocities of the PS particles in the x and y directions could be calculated. By following this procedure at different experimental settings, the dependencies of the ratcheting on the frequency of chopping of 980 nm excitation and its intensity could be studied experimentally.

Prior to each such experiment, the 980 nm laser was blocked, to allow the recording of the PS spheres' Brownian motion; this was done to ensure that no drifts were present in the system due to e.g. sample tilting or thermal/concentration gradients. Upon confirmation of normal Brownian motion, the laser was unblocked and the power of the laser was increased until the PS spheres were trapped by the plasmonic ratchets. For 40 nm PS spheres, an

incident intensity of 0.47 kW cm^{-2} was found to be sufficient to provide a stable trapping of the particles. At this point, the chopping of the 980 nm laser excitation could be initiated in order to investigate the effect of the periodic application of a plasmonic potential on the PS sphere motion. A 10-slot chopping blade with a 50% duty cycle was used for the purpose, allowing for a simple conversion between the frequency of chopping blade rotation, f , and the time that the potential remained off during each on-off cycle of the chopping,

$$\tau_{off} = \frac{1}{20f}. \quad (4)$$

Figure 6(a) shows the x and y components of the mean velocities of PS spheres being driven by our plasmonic ratchet, with the 980 nm illumination chopped at frequencies corresponding to τ_{off} between 4 and 8.5 ms. As the graph shows, no net PS particle motion was observed outside of τ_{off} range of 4.7 – 6.7 ms, whereas within this range some net motion along both x and y direction occurred. The motion was strongly directed along the y axis, with the y -component of the mean velocity being a factor of ~ 20 larger than the x -component. These observations firmly confirm the rectification of Brownian motion of PS spheres as the source of their net motion, since the motion had a strong preferential direction that was aligned with the ratchet central axis and it only occurred within a narrow range of τ_{off} values, that matched the τ_{off} range predicted theoretically (4.6–6.7 ms, Table 1). Other sources of net motion of PS particles, such as thermal drifts and concentration gradients, would instead have resulted in a constant mean displacement of PS particles that would be independent of the chopping frequency of the 980 nm illumination.

Further confirmation of ratcheting of PS spheres by the designed plasmonic structures could be obtained from the dependency of the motion of PS spheres on the intensity of 980 nm illumination. This is because ratcheting is dependent on the efficiency of the analyte trapping during the potential-on stages of the process, with inefficient trapping leading to a reduction in the rectification of particle motion. Figure 6(b) shows the results of

investigations involving the ratcheting of 40 nm PS spheres at different intensities of chopped 980 nm illumination ($\tau_{off} = 5.5$ ms). As can be seen in this figure, and in agreement with theory, no bias in the motion of PS spheres is observed for intensities below ≈ 0.5 kW cm⁻², which corresponds to the onset value where the depth of the trapping potential becomes greater than the thermal energy of the system and therefore the trapping of the particles becomes possible, allowing for the ratcheting process to occur. As the intensity of the illumination was increased above this onset, the trapping of the PS spheres became more efficient and therefore the ratcheting of the particles improved, causing a more obvious difference in the motion along the y and x directions.

However, above 0.8 kW cm⁻² illumination intensity the ratcheting efficiency started to decrease and above 1.5 kW cm⁻² no ratcheting was observed. One possible cause for the observed decrease is an onset of thermophoretic effects, whereby continued illumination of plasmonic antennas causes local generation of heat, establishing thermal gradients in their vicinity that act against the trapping optical forces. Since such effects are common in plasmonic systems, the heating of the aqueous environment by the plasmonic ratchet was tested under CW 980 nm illumination. Results showed that the temperature increase was minimal, less than 1°C over a 1-hour illumination period, even at an intensity of 2.4 kW cm⁻². Despite the likelihood of higher local temperatures around the antennas than those observed globally,^{28,29} this result suggests that thermal effects are minimal at the powers used to operate our ratchet. Consequently, they cannot be responsible for the observed decrease in ratcheting efficiency, suggesting that other mechanisms must be influencing the system's performance at higher illumination intensities.

Trapping efficiency measurements, shown in 6(b), further support this conclusion. The traps become stiffer with increasing illumination powers and continue to do so even beyond the onset of decreased ratcheting efficiency discussed previously. This indicates that the trapping mechanism itself remains effective at higher illumination powers. A more likely cause of the decreased efficiency is the increased adherence of particles to the surface of the

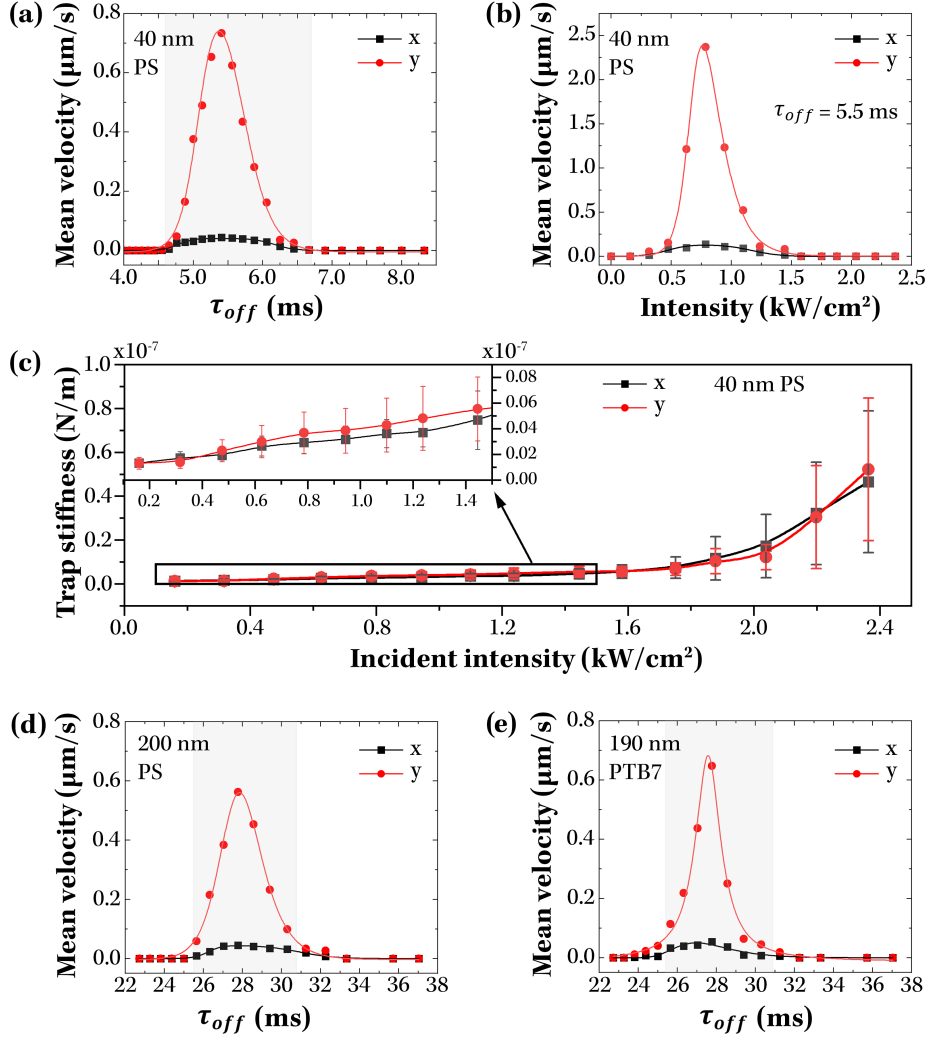


Figure 6: The mean velocities achieved during ratcheting of 40 nm PS spheres as a function of (a) the time the periodic potential remained off (t_{off}) and (b) the incident excitation intensity, for $t_{off} = 5.5$ ms. In panel (a), the incident excitation intensity was 0.47 kW cm^{-2} and the shaded region indicates the theoretically-predicted range of τ_{off} values where ratchetting of 40 nm PS spheres could be achieved. Ratchetting characteristics. (c) Trap stiffness of plasmonic structures under CW illumination. Inset shows data obtained at low incident intensities. (d) and (e) show the mean velocities achieved during ratcheting of 200 nm PS and PTB7 spheres as a function of time the periodic potential remained off (τ_{off}). In panel (a), the incident excitation intensity was 0.47 kW cm^{-2} , whereas for panels (d) and (e), the excitation intensities were approximately 2.5 kW cm^{-2} . The shaded regions in panels (a), (d) and (e) indicate the theoretically-predicted range of τ_{off} values for successful ratchetting of particle of specified sizes and compositions.

ratchets. At higher powers, more and more particles are driven to ratchet surfaces by the strong electric field gradients, and an increasingly larger proportion of particles then adhere

to said surfaces *via* van der Waals forces, resulting in an overall reduction of the particles' net velocity. This adherence effect explains the observed decline in ratcheting efficiency at higher illumination intensities, and eliminates thermal increases as the source of decreased ratcheting efficiency.

Ratcheting of particles with different sizes and compositions

To further investigate the versatility and robustness of our plasmonic ratchet system, we conducted tests on polystyrene nanospheres of larger sizes (200 nm in diameter). Although the ratchets were designed and optimised for 40 nm PS spheres, ratcheting behaviour could still be obtained for 200 nm spheres, as evidenced by the much larger mean velocities of spheres along the y direction (the ratcheting axis) compared to the x direction (Figure 6(d)). The maximum velocities obtained were lower for the 200 nm PS spheres ($1.55 \mu\text{m s}^{-1}$) than for the 40 nm spheres ($2.37 \mu\text{m s}^{-1}$), which is expected due to the slower diffusion of the former (as per Eq.3). Additionally, for the 200 nm spheres, ratcheting occurred at a different range of τ_{off} values, with the range centered at 27.7 ms as opposed to 5.5 ms for 40 nm spheres. This large change in τ_{off} values is due to a combination of the slower diffusion of the spheres and the less efficient trapping of the larger particles. The electric field gradients experienced by the 200 nm spheres are effectively “averaged out” over their entirety, resulting in larger electric forces but shallower and less asymmetric trapping potentials (Figure S5 in SI) compared to 40 nm PS spheres. Theoretical calculations, which account for both of these effects through Equations 1-3, predict a ratcheting range of 25.5 – 30.8 ms for the 200 nm spheres (Table 1), which aligns well with our experimental results.

Building upon these studies, we further examined the adaptability of our plasmonic ratchet system by investigating its capability to handle particles with different compositions. To determine whether material properties could influence the ratcheting efficiency, experiments were conducted to compare the behaviour of nanoparticles of approximately 200 nm diameter made from different materials. The nanoparticle systems chosen for these inves-

Table 1: Effect of nanoparticle size and composition on their ratcheting characteristics.

Particle composition	Polystyrene	Polystyrene	PTB7
Particle size	40 nm	200 nm	190 nm
Maximum mean velocity, x ($\mu\text{m s}^{-1}$)	0.14	0.06	0.15
Maximum mean velocity, y ($\mu\text{m s}^{-1}$)	2.37	1.61	1.84
Optimum experimental t_{off} , (ms)	5.5	27.7	27.7
Theoretical t_{off} range, (ms):	4.6 – 6.7	25.5 – 30.8	25.4 – 30.9

tigations were 200 nm PS spheres and 190 nm nanoparticles made from PTB7 conjugated polymer (poly[[4,8-bis[(2-ethylhexyl)oxy]benzo[1,2-b:4,5-b']dithiophene-2,6-diyl] [3-fluoro-2-[(2-ethylhexyl)carbonyl]thieno[3,4-b]thiophenediyl]]), stabilized by pluronic F127 amphiphilic copolymer (see section 2.2.1 of SI for fabrication information). Given the similar sizes of the particles and thus also the diffusion rates (Equation 3)), both the trapping forces/potentials and the τ_{off} range where ratcheting could be observed were all expected to be similar (SI Figures S5–S7 and Table 1).

As anticipated, ratcheting was observed for both PS and PTB7 particles, with the τ_{off} range remaining approximately the same for both and aligning well with the theoretically-predicted values given in Table 1. Interestingly, at optimum chopping frequency, slightly higher velocities were obtained for the PTB7 spheres ($1.84 \mu\text{m s}^{-1}$) compared to the PS spheres ($1.55 \mu\text{m s}^{-1}$), as shown in Figure 6(e) and (d). This difference is likely entirely due to the slightly smaller sizes and faster diffusion rates of the PTB7 particles, as any differences in trapping potentials and forces between the two theoretically should not influence their net motion since particles are only able to translate during the periods when the potential is off. These findings underscore the adaptability of the plasmonic ratchet system, demonstrating efficient ratcheting behavior across various particle sizes and compositions, thereby highlighting its potential for broad applications in nanoparticle manipulation.

Conclusions

This study demonstrates that plasmonic ratchet systems provide a highly effective means for the controlled long-range transport of nanoscale particles. By leveraging the asymmetric geometry of plasmonic structures and external optical modulation, the ratchet design was optimized for 40 nm PS spheres, fabricated and then implemented experimentally to achieve efficient rectification of Brownian motion of 40 nm spheres. The plasmonic ratchet described in this work is easily fabricated using well-established nanofabrication techniques, and the experimental setup for exciting the plasmonic modes and tracking of analytes is both simple and efficient. Furthermore, the system’s versatility was highlighted through successful ratcheting of larger 200 nm PS spheres and 190 nm PTB7 nanoparticles, maintaining efficient performance across different nanoparticle sizes and compositions.

Notably, the plasmonic ratchet system developed here could be operated at low powers ($\sim 0.785 \text{ W m}^{-2}$) to achieve high net analyte transport velocities of up to $2.4 \mu\text{m s}^{-1}$ for the 40 nm PS spheres and $\sim 0.6 \mu\text{m s}^{-1}$ for the larger 200 nm PS and PTB7 particles. This represents a marked improvement over previous optical ratchet designs enabling the rectification of brownian diffusion of nanoscale particles. For example, silicon photonic crystal slabs with assymetric features, developed by Wu S.-H. *et al.*, achieved transport speeds of $1 \mu\text{m s}^{-1}$ for 520 nm PS spheres, but required much higher coupled power densities of (10^8 W m^{-2}).¹⁹ Lee S.-H. *et al.* used a holographic optical tweezers technique to create a large-scale potential energy landscape that could be dynamically modulated.²² They successfully ratcheted $1.5 \mu\text{m}$ colloidal silica spheres, but achieved relatively low transport speeds of $\sim 0.01 \mu\text{m s}^{-1}$ and required 3.5 mW of optical power per trap to do so. Assuming that waist of each trap width was similar to the size of the particles being ratcheted, this corresponded to trapping intensities of $\sim 10^8 \text{ W m}^{-2}$. Finally, Faucheux L. P. *et al.* used a strongly focused infrared laser to create an optical trap that was then moved along a circle using two oscillating translating mirrors, that was then synchronised to the rotation of a neutral density filter in order to modulate the strength of the optical trap during its rotation.¹⁵ This ratcheting

system achieved maximum translation velocities of $\sim 0.1 \mu\text{m s}^{-1}$ for $1.5 \mu\text{m}$ silica spheres, but necessitated an at-sample intensity of $\sim 10^{14} \text{ W m}^{-2}$. The use of high optical powers can lead to several detrimental consequences for the analytes being transported. First of all, elevated power levels increase the risk of thermal damage. For example, in viral particles, protein denaturation and disruption of the viral envelope structure can both ensue.^{30,31} Additionally, high intensities can cause photodamage, potentially generating reactive oxygen species or other harmful byproducts that can compromise the viability and integrity of viral particles.³¹ Such damages can lead to inaccuracies in viral load quantification and diagnostic assays by affecting the detectability and measurable properties of the viruses. In contrast, the lower power requirements of our plasmonic ratchet system mitigate these risks, making it a safer and more reliable tool for applications involving delicate viral samples.

These results emphasize the potential of plasmonic ratchets as a robust, scalable, and energy-efficient solution for the transport and manipulation of nanoscale analytes, particularly in lab-on-a-chip and microfluidic devices, where precise and efficient transport is crucial. The ability to manipulate various analytes with high control and minimal power consumption makes this system highly suitable for applications in the life sciences, such as moving and sorting viral particles and disease diagnostics.

Experimental

Numerical simulations

The optical response of the plasmonic ratchet array was simulated using the radio-frequency package of COMSOL Multiphysics. The array of structures shown in Figure 2(a) was modelled under plane wave excitation, and using periodic boundary conditions. The refractive index of the quartz substrate was taken to be 1.5, and the refractive indices of gold (Au) and chromium (Cr) at the excitation wavelength were taken from references 32 and 33, respectively. Using the results of the simulations, the scattering (σ_{sca}) and absorption (σ_{abs})

cross-sections of the arrays were calculated by normalizing the total intensities scattered and absorbed by the plasmonic structures by that of the incident plane wave. The extinction cross-sections were then obtained from $\sigma_{ext} = \sigma_{sca} + \sigma_{abs}$.²⁵ Furthermore, using the results of these simulations, the forces experienced by extremely small spherical particles above and in the near-fields of the plasmonic ratchets could be calculated using the dipolar approximation, according to:

$$\vec{F}(\vec{r}) = \frac{\Re[\alpha(\omega)]}{4} \nabla \vec{E}(\vec{r}) \quad (5)$$

where $\nabla \vec{E}(\vec{r})$ is the gradient of the electric field at position of interest \vec{r} and $\alpha(\omega)$ is the particle's polarizability, defined as:

$$\alpha(\omega) = 4\pi r^3 \frac{\varepsilon_m(\omega) - \varepsilon_p(\omega)}{\varepsilon_m(\omega) + 2\varepsilon_p(\omega)}. \quad (6)$$

Here, ε_m and ε_p are the relative permittivities of the suspending medium and the spherical particle, respectively, and r is the radius of the particle.

Alternatively, a more accurate determination of the optical forces experienced by the spherical particle could be performed. These involved performing simulations that included the dielectric spherical particles in the vicinity of plasmonic ratchets and subsequent calculation of forces *via* an integration of the time-averaged Maxwell Stress Tensor, $\langle \overleftrightarrow{\mathbf{T}}(\vec{r}, t) \rangle$, over a cubic surface containing the particle:

$$\vec{F}(\vec{r}) = \int_{\delta V} \langle \overleftrightarrow{\mathbf{T}}(\vec{r}, t) \rangle \cdot \vec{n}(\vec{r}) da \quad (7)$$

where $\vec{n}(\vec{r})$ is the normal to the integration surface at position \vec{r} . To avoid meshing-related errors, the side-length of the cube over which the integration was performed was 4 nm larger than the diameter of the particle it contained. For these purposes, material constants of PS and PTB7 polymers were taken from.^{34,35}

Using the results of Equations 5 or 7, the potential energy of the particle at a specific

position above the ratchet, \vec{r} , relative to a reference position, \vec{r}_{ref} , could then be determined by integrating the optical forces acting on the particle along a straight line between the two points:

$$U(\vec{r}) = \int_{\vec{r}_{ref}}^{\vec{r}} \vec{F}(\vec{r}') \cdot d\vec{r}' \quad (8)$$

Typically, the reference position was taken to be the geometrical centre of the space between two adjacent ratchet units.

Fabrication of plasmonic ratchets

Arrays of plasmonic structures were fabricated using standard e-beam lithography methods, using 180 nm of 950K A4 Poly(MethylMethacrylate) (MicroChem) as the resist, pre-baked at 180°C for 3 minutes. E-beam write was performed on an e-LINE Plus (Raith) EBL using 20 kV accelerating voltage, 10 μm aperture and 10 μm working distance. Post-write, the resist was developed for 30 seconds in 1:3 methyl isobutyl ketone:isopropyl alcohol (IPA), followed by a further 30 seconds wash in pure IPA. Following development, 5 nm of Cr and 45 nm of Au were evaporated on top of the resist, at a rate of 0.2 \AA s^{-1} and 2 \AA s^{-1} respectively, using the Amod System evaporator (Angstrom Engineering). Finally, lift-off was performed by immersing the substrate into acetone for 24 hours, followed by rinsing with IPA and deionised water.

Particle tracking

Substrates containing plasmonic ratchets were placed into the sample holder fitted to a Nikon Ti-U2 microscope. A small drop of a dielectric particle dispersion (PS or PTB7 beads, 1:10 v/v in water) was placed directly on top of the ratchet array. Sample was illuminated using side-illumination from a white-light source (OSL2, Thorlabs) and light scattered by the dielectric spheres was collected from the other side of the sample using a 40x objective (Nikon, CFI Super Fluor). The scattered light was recorded using KURO sCMOS camera

(Princeton Instruments).

To trap the particles, sample was illuminated with a collimated 980 nm CW laser radiation (1.4–3.7 mW, MDL-III-980High Stability Infrared Laser, CNI Laser), incident onto the sample from the top. A 650 nm short-pass filter (ThorLabs) was used to exclude this radiation from recorded images. Chopping of the trapping laser was performed using MC2000B optical chopper (ThorLabs), fitted with a 50%-duty blade.

Videos of at least 3500 frames recorded by the camera were exported as .tiff files and analysed using an own code. Briefly, a video of a specific measurement was imported and the first frame from the video was used to set the xy axis for the analysis, to account for any rotation of the sample in the sample holder. This was done by showing the first frame to the user, who manually drew a line on the image such that it aligned with the edge of the ratchet array. Each frame of the video was then pre-filtered using either a band-pass filter (Python) or using morphological operations (Matlab), in order to eliminate extremely small features (*i.e.* noise) and remove background. For each frame, positions and sizes of each particle were identified (in the new reference frame) by detecting all maxima in the image and iteratively applying a circular mask to the image (Python) or by applying blob analysis (Matlab). Results were filtered by applying morphological operations to exclude particles with sizes above and brightness below a certain threshold, corresponding to removal of data from aggregates of nanoparticles. The positions of particles were then linked from frame to frame, by generating pair-wise associations of particle positions that resulted in a minimum square displacement of all particles from frame to frame. For each identified particle, the code yielded tracks in the form of (x, y, t) data, some of which are shown in Figure 5(d).

To generate displacement versus time box plots shown in Figure 5(b) and (c), for each time point on the graph, tracks were first filtered to remove those of insufficient time length. For the remainder, tracks were cropped to the specified time, and net displacement for each particle was calculated by subtracting its initial position from the final position. The resulting set of displacements was saved, and the process was repeated for other time points.

The saved data were then analysed statistically and plotted as box plots using OriginLab. The net displacement versus time data was fitted to a linear model to yield the mean velocity of the particles in x and y directions. This analysis was repeated for videos obtained at different settings (e.g. different chopping frequencies or different illumination intensities), to yield the corresponding mean velocity versus τ_{off} or intensity graphs shown in Figure 6.

To evaluate the stiffness of the traps offered by the plasmonic ratchet structure, motion of 40 nm PS particles was recorded at different 980nm laser intensities. Videos were evaluated as above to obtain the net displacement ($\sigma_{x,y}$) of particles in x and y directions over a 45 s time period. The data was then used to calculate the trap stiffness of the ratchet structure in the corresponding directions ($k_{x,y}$) according to $k_{x,y} = k_b T / \sigma_{x,y}^2$.^{36,37}

Acknowledgement

M.P.C., A.M.D. and A.R. acknowledge the funding support from the Royal Society (RGF\R1\180068, UF150542, URF\R\211023) and from EPSRC (EP/W017075/1). S.A.M. acknowledges the Lee-Lucas Chair in Physics. P.A.H. acknowledges the MICIU and AEI (RYC2021-031568-I and “María de Maeztu” Programme for Units of Excellence in R&D, CEX2023-001316-M). D.R. acknowledges ERC iCOMM 789340 for the funding support.

Supporting Information Available

Additional details on numerical simulations, including optimization of ratchet asymmetry, Maxwell Stress Tensor calculations, optimization of ratchet periodicity and additional numerical results for 200 nm PS and PTB7 particles. Additional ratcheting data for 200 nm PS and PTB7 nanoparticles are also provided.

References

- (1) Favre-Bulle, I. A.; Stilgoe, A. B.; Scott, E. K.; Rubinsztein-Dunlop, H. Optical trapping in vivo: theory, practice, and applications. *Nanophotonics* **2019**, *8*, 1023–1040.
- (2) Svoboda, K.; Block, S. M. Biological applications of optical forces. *Annual review of biophysics and biomolecular structure* **1994**, *23*, 247–285.
- (3) Neuman, K. C.; Block, S. M. Optical trapping. *Rev. Sci. Instrum.* **2004**, 2787–809.
- (4) Grier, D. A revolution in optical manipulation. *Nature* **2003**, *424*, 810–816.
- (5) Paiva, J. P. A. S. R. R. S. R. I., J. S. iLoF: An intelligent Lab on Fiber Approach for Human Cancer Single-Cell Type Identification. *Sci. Rep.* **2020**, *10*.
- (6) Polimeno, P.; Magazzù, A.; Iatì, M. A.; Patti, F.; Saija, R.; Esposti Boschi, C. D.; Donato, M. G.; Gucciardi, P. G.; Jones, P. H.; Volpe, G.; Maragò, O. M. Optical tweezers and their applications. *Journal of Quantitative Spectroscopy and Radiative Transfer* **2018**, *218*, 131–150.
- (7) Binsley, J. L.; Martin, E. L.; Myers, T. O.; Pagliara, S.; Ogrin, F. Y. Microfluidic devices powered by integrated elasto-magnetic pumps. *Lab Chip* **2020**, *20*, 4285–4295.
- (8) Liu, C.; Hu, G. High-Throughput Particle Manipulation Based on Hydrodynamic Effects in Microchannels. *Micromachines* **2017**, *8*, 73.
- (9) Ashkin, A.; Dziedzic, J. M. Optical trapping and manipulation of viruses and bacteria. *Science* **1987**, *235*, 1517–1520.
- (10) Sanavio, B.; Krol, S. On the Slow Diffusion of Point-of-Care Systems in Therapeutic Drug Monitoring. *Frontiers in Bioengineering and Biotechnology* **2015**, *3*, 20.
- (11) Magnasco, M. O.; Stolovitzky, G. Feynman’s Ratchet and Pawl. *Journal of Statistical Physics* **1998**, *93*.

- (12) Byun, A.-S. K. C. Y. K. T. S., C. K. Pumps for microfluidic cell culture. *Electrophoresis* **2014**, *35*, 245–257.
- (13) Rousselet, S. L.-A. A. P. J., J. Directional motion of brownian particles induced by a periodic asymmetric potential. *Nature* **1994**, *370*, 446–447.
- (14) Bader, H.-R. W. H. S. A. D. M. W. M. G. A. B. J. M. S. J. W. M. G. T. R. J. M., J. S. DNA transport by a micromachined Brownian ratchet device. *Proceedings of the National Academy of Sciences of the United States of America* **1999**, *96*, 13165–13169.
- (15) Faucheux, L. P.; Bourdieu, L. S.; Kaplan, P. D.; Libchaber, A. J. Optical Thermal Ratchet. *Phys. Rev. Lett.* **1995**, *74*, 1504–1507.
- (16) Astumian, R. D. Thermodynamics and Kinetics of a Brownian Motor. *Science* **1997**, *276*, 917–922.
- (17) van Oudenaarden, B.-S. G., A. Brownian ratchets: molecular separations in lipid bilayers supported on patterned arrays. *Science* **1999**, *285*, 1046–1048.
- (18) Lee, S.-H.; Ladavac, K.; Polin, M.; Grier, D. G. Observation of Flux Reversal in a Symmetric Optical Thermal Ratchet. *Phys. Rev. Lett.* **2005**, *94*, 110601.
- (19) Near-Field, On-Chip Optical Brownian Ratchets. *Nano Lett.* **2016**, *16*, 5261–5266.
- (20) Semeraro, M.; Gonnella, G.; Lippiello, E.; Sarracino, A. Diffusion Properties of a Brownian Ratchet with Coulomb Friction. *Symmetry* **2023**, *15*, 200.
- (21) Spiechowicz, J.; Marchenko, I. G.; Hänggi, P.; Łuczka, J. Diffusion Coefficient of a Brownian Particle in Equilibrium and Nonequilibrium: Einstein Model and Beyond. *Entropy* **2023**, *25*, 42.
- (22) Lee, S.-H.; David G, G. One-dimensional optical thermal ratchets. *J. Phys.: Condens. Matter* **2005**, *17*, S3685.

- (23) Huidobro, P. A.; Ota, S.; Yang, X.; Yin, X.; Garcia-Vidal, F. J.; Zhang, X. Plasmonic Brownian ratchet. *Phys. Rev. B* **2013**, *88*, 201401.
- (24) Liao, H.-Z. T. W. C. H. G. N. T. H. H. J. C. C. K. P., J. W.; Lu, T. C. Highly Localized Surface Plasmon Nanolasers via Strong Coupling. *Nano letters* **2023**, *23*, 4359–4366.
- (25) Giannini, F.-D.-A. I. H. S. C. M. S. A., V. Plasmonic nanoantennas: fundamentals and their use in controlling the radiative properties of nanoemitters. *Chemical reviews* **2011**, *111*, 3888–3912.
- (26) Barnes, D.-A.-E. T., W. Surface plasmon subwavelength optics. *Nature* **2003**, *424*, 824–830.
- (27) Maier, S. *Plasmonics - Fundamentals and Applications*; Springer, 2007.
- (28) Anyika, T.; Hong, C.; Ndukaife, J. C. High-speed nanoscale optical trapping with plasmonic double nanohole aperture. *Nanoscale* **2023**, *15*, 9710–9717.
- (29) Ndukaife, K.-A. V. N. A. G. S. V. M. W. S. T. B. A., J. C. Long-range and rapid transport of individual nano-objects by a hybrid electrothermoplasmonic nanotweezer. *Nature nanotechnology* **2016**, *11*.
- (30) Burrell, C. J.; Howard, C. R.; Murphy, F. A. In *Fenner and White's Medical Virology*, fifth edition ed.; Burrell, C. J., Howard, C. R., Murphy, F. A., Eds.; Academic Press: London, 2017.
- (31) Rath, S. L.; Kumar, K. Investigation of the Effect of Temperature on the Structure of SARS-CoV-2 Spike Protein by Molecular Dynamics Simulations. *Frontiers in Molecular Biosciences* **2020**, *7*.
- (32) Johnson, P. B.; Christy, R. W. Optical Constants of the Noble Metals. *Phys. Rev. B* **1972**, *6*, 4370–4379.

- (33) Johnson, P. B.; Christy, R. W. Optical constants of transition metals: Ti, V, Cr, Mn, Fe, Co, Ni, and Pd. *Phys. Rev. B* **1974**, *9*, 5056–5070.
- (34) Nina G. Sultanova, I. N., S. Kasarova Dispersion Properties of Optical Polymers. *Acta Physica Polonica Series a* *116*.
- (35) C. Stelling, M. K. T. A. F. K. M. T. M. R., C. R. Singh Plasmonic nanomeshes: their ambivalent role as transparent electrodes in organic solar cells. *Sci. Rep.* **2017**, *7*, 42530.
- (36) aterston J. J.; William, S. J. I. On the physics of media that are composed of free and perfectly elastic molecules in a state of motion. *Philosophical Transactions of the Royal Society of London A* **1892**, 1831–1879.
- (37) Boltzmann, L. *Vorlesungen über Gastheorie: Th. Theorie van der Waals'; Gase mit zusammengesetzten Molekülen; Gasdissociation; Schlussbemerkungen*: Leipzig, 1898.

Supplementary Information

Numerical Simulations

Optimization of ratchet asymmetry via dipole approximation

Numerical simulations of the optical response of ratchet structures under plane wave 980 nm illumination were performed using the RF module of COMSOL Multiphysics. Simulations on individual (single unit cell) structures were performed using a large domain size, with Perfectly Matched Layers (PMLs) as its boundaries; this was done to avoid any reflections from the domain boundaries contributing to results of the simulations.

Structures with asymmetry degrees varying from 0° to 21° were considered, in 3° steps, with the asymmetry degree being defined as the angle θ in Figure 2(a) of the main text. From the simulated electric fields, examples of which are shown in Figure 7(b), optical forces offered by each structure were calculated using the dipole approximation,^[S1] which assumes that diffusing particles can be approximated to be small dipoles of dimensions much smaller than the excitation wavelength and with homogeneous fields inside of them:

$$F = \frac{\Re[\alpha(\omega)]}{4} \nabla E(r) \quad (9)$$

with $\alpha(\omega)$ being the particle's polarizability, defined as:

$$\alpha(\omega) = 4\pi r^3 \frac{\varepsilon_m(\omega) - \varepsilon_d}{\varepsilon_m(\omega) + 2\varepsilon_d} \quad (10)$$

where ε_m and ε_d are the relative permittivities of the medium and of the particle respectively, r is the particle radius and $\nabla E(r)$ is the gradient of the electric field. By integrating these forces along the axis of symmetry of the ratchetting structure, using Equation (8) of the main text, trapping potentials were calculated 10nm above the top surface of the ratchet structure. Results of these calculations are shown in Figure 7. Based on these results,

asymmetry degree of $\sim 9^\circ$ was deemed to be optimum, as it provided a deep, extended and most asymmetric potential.

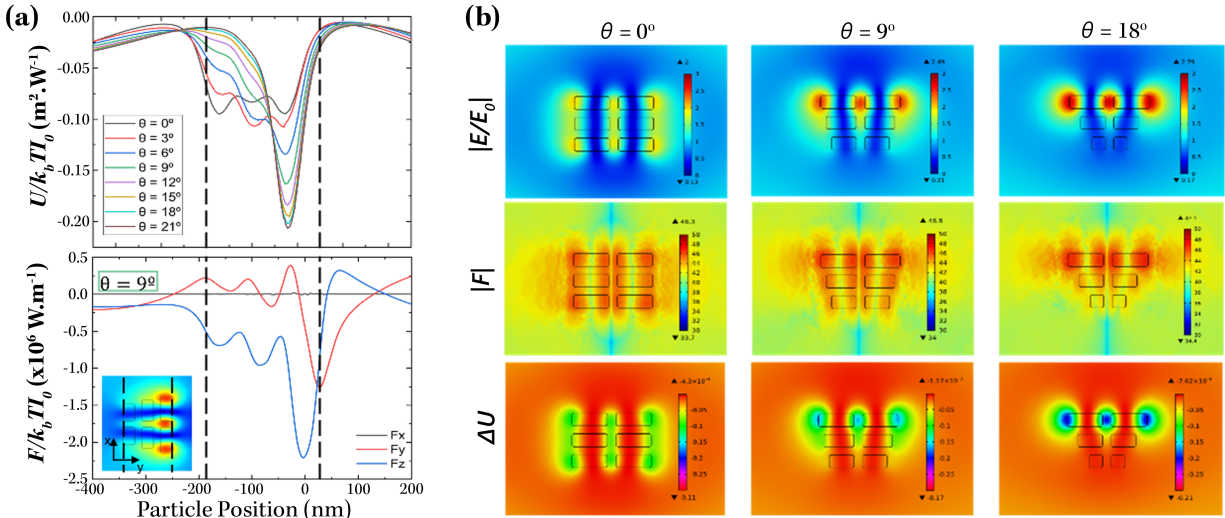


Figure S 7: Optimization of ratcheting structure unit cell asymmetry, under dipolar approximation. Top graph of panel (a) shows the trapping potentials for different structure asymmetry degrees θ . Bottom graph of panel (a) shows the x , y and z components of the optical forces generated by the ratcheting unit cell structure of optimum asymmetry degree ($\theta = 9^\circ$). Panel (b) shows electric fields, optical forces and trapping potential profiles for a few select asymmetry degrees of plasmonic ratchet unit cell structures.

Maxwell Stress Tensor calculations of optical forces and potentials

In the study involving optimization of the periodicity of the ratchet (described in the main text), as well as the theoretical predictions of ratchet behavior for nanoparticles of different sizes and compositions, the Maxwell Stress Tensor (MST) method was used to fully account for the effect that the polarization of analyte particle had on the electric fields in its vicinity. To perform these calculations, a set of numerical simulations of the optical response of the ratchet to normally-incident plane wave of 980 nm were performed, with a single dielectric sphere placed at different positions along the central axis and 10 nm above the surface of the ratchet (measured from the top of the ratchet surface to the bottom of the sphere). Periodic boundary conditions were used to simulate an infinite array of the system. For the dielectric sphere, material properties used were those corresponding to either the polystyrene

or the PTB7 polymer, as appropriate. The position of the sphere was changed between each simulation, along the ratcheting axis (y direction, see Figure 8), to yield y -distance dependent series of results.

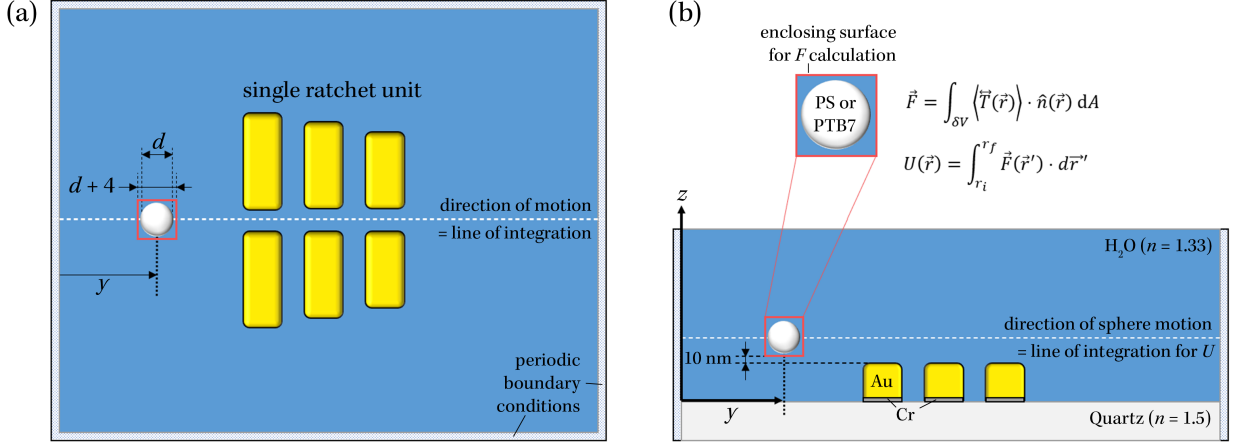


Figure S 8: Simulation space set-up for calculations of optical forces and potentials using the Maxwell Stress Tensor, showing the system (a) from the top and (b) from the side. Calculation of trapping potential involved a series of simulations, with varying positions y of the analyte sphere of diameter d , along the ratchet axis (white dashed line) and a height of 10 nm above the top surface of the ratchet. Maxwell Stress Tensor was calculated from the fields yielded by the simulations and then integrated over the surface enclosing the sphere (red solid box), of side length $d + 4$ nm. In all simulations, ratchets were on a quartz substrate and in water. The dimensions and design of the ratchet is described in the main text. Periodic boundary conditions were used to simulate an infinite array of plasmonic ratchets.

For each simulation in the series, i.e. for each position of the sphere above the ratchet, MST was calculated using:^[S1,S2]

$$\overleftrightarrow{T}(\vec{r}, t) = \left[\varepsilon_0 \varepsilon \vec{E} \vec{E} + \mu_0 \mu \vec{H} \vec{H} - \frac{1}{2} (\varepsilon_0 \varepsilon E^2 + \mu_0 \mu H^2 \overleftrightarrow{I}) \right] \quad (11)$$

where ε and μ are the permittivity and permeability of the surrounding medium.

The optical force exerted on a sphere was then calculated by integrating MST over an arbitrary surface δV enclosing the sphere:

$$\vec{F}(\vec{r}) = \int_{\delta V} \langle \overleftrightarrow{T}(\vec{r}, t) \rangle \cdot \hat{n}(\vec{r}) da \quad (12)$$

where $\hat{n}(\vec{r})$ is the unit vector normal to the surface at position \vec{r} and pointing outwards from the enclosed volume. Integration was performed over a cubic surface, centered at the dielectric sphere's center and of side length 4 nm larger than the sphere's diameter.

These calculations yielded a set of (F_x, F_y, F_z) as a function of sphere position above and along the central axis of the ratchet, y . The trapping potential along this direction could then be calculated *via* integration:

$$U(y) = \int_0^y F_y(y') dy' \quad (13)$$

where the lower limit of integration of $y = 0$ corresponded to the mid-point between two adjacent cells (due to the periodic nature of the structure).

Optimization of ratchet periodicity

Using methods described above, the periodicity of the ratchet array was optimized to yield deepest trapping potentials. This was achieved by first performing a series of simulations where the yz boundaries of the simulation space had PMLs applied to them, whilst periodic boundary conditions were applied to the xz boundaries, thus simulating a chain of ratcheting structures, repeated along y direction. The spacing between the ratchets in the chain was controlled by the size of the simulation domain along the y direction, and this was varied between 400 and 1000 nm. These variations caused very strong changes in the optical response of the ratchet, with periodicity of 700 nm for the y -direction offering by far the strongest electric field enhancements, optical forces and trapping potentials (Figure 9).

To determine the optimum periodicity in the x -direction, periodic boundary conditions were additionally applied to the yz boundaries, and the length of the domain along the x direction was varied between 750 and 1000 nm. Variations in the electric fields, optical forces and potentials were very subtle in this case (Figure 10); nonetheless, x -period of 800 nm performed marginally better than other periodicity and was therefore deemed optimum.

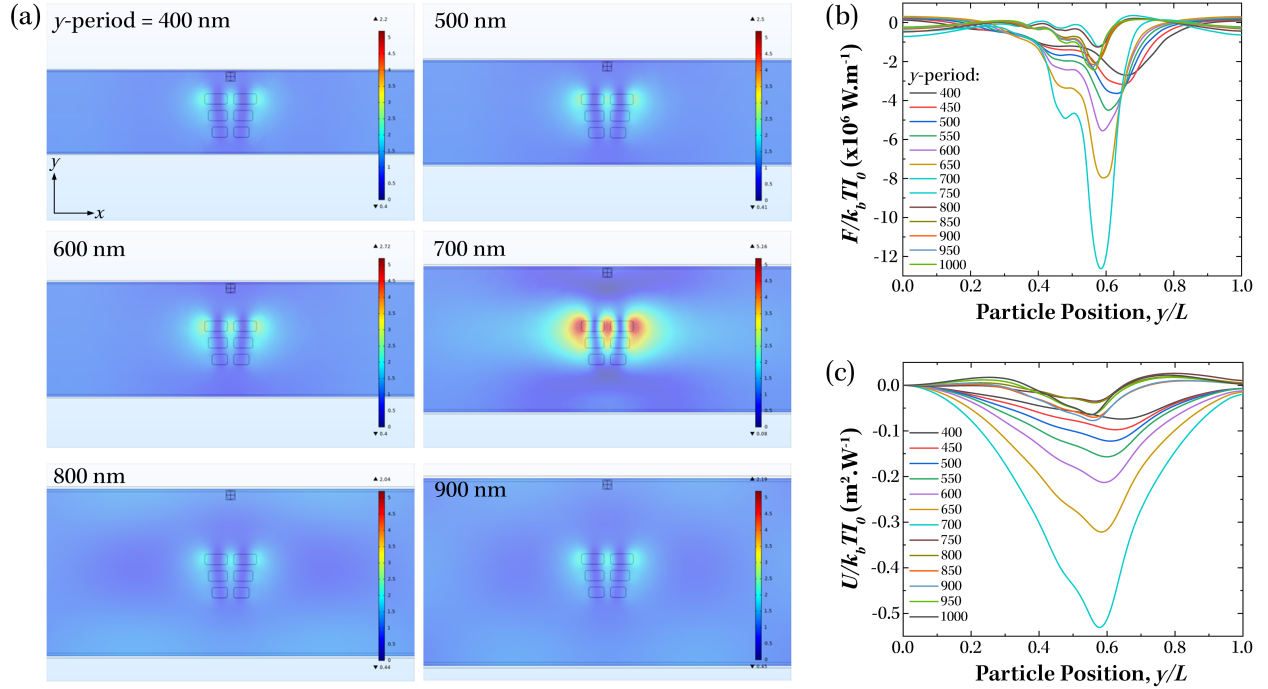


Figure S 9: Optimization of y -period of ratchet array using numerical simulations involving a chain of ratchet unit cells, with the period of the unit cell varying between 400 and 1000 nm. (a) Electric field enhancements (E/E_0) above ratchet structures, in the presence of 40 nm polystyrene sphere located 10nm above the ratchet surface. The profiles are taken at a height cutting through the middle of the sphere ($z = 80$ nm) above the substrate. All profiles are plotted using the same colorscale of $\log_{10}(E/E_0) = 0$ to 5. (b) and (c) show z -component of the optical force and potentials experienced by the polystyrene sphere as a function of its position y along the central axis of the ratchet. In panels (b) and (c), the particle position is plotted in relative units of its displacement from the mid-point of two ratchets to the total length of the ratchet unit cell, L .

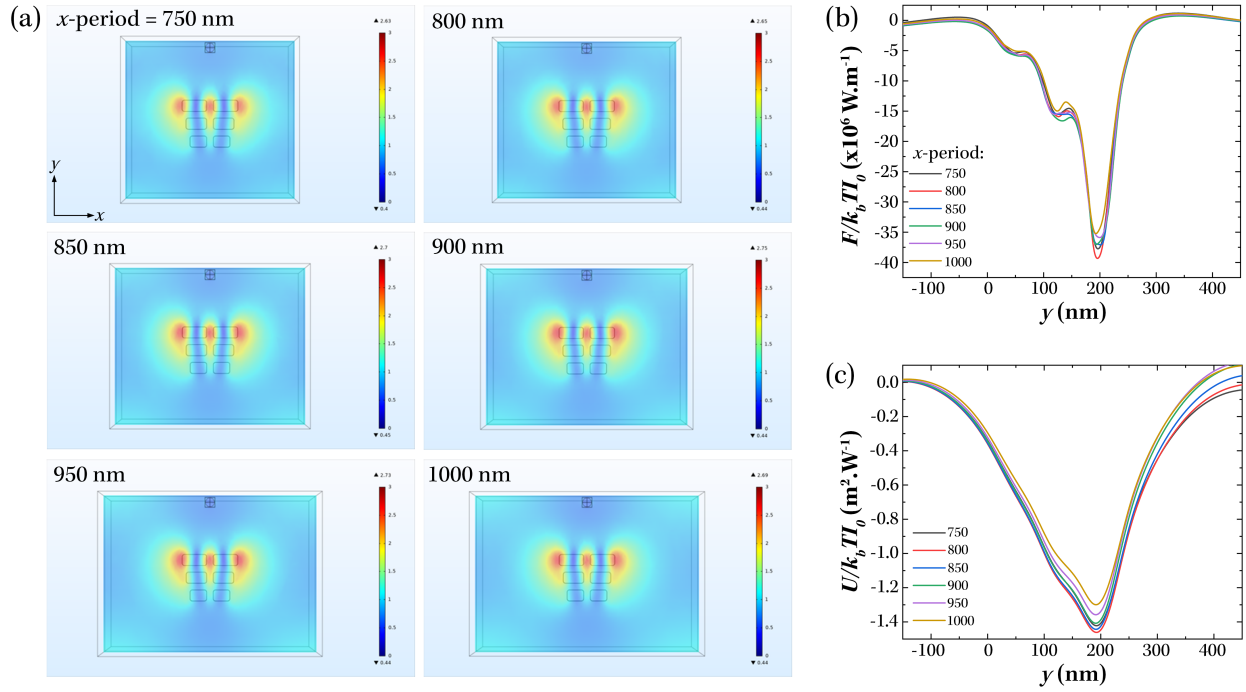


Figure S 10: Optimization of x -period of ratchet array using numerical simulations involving an array of ratchets with the y -period set to 700 nm and x -period varied between 750 and 1000 nm. (a) Electric field enhancements (E/E_0) above ratchet structures, in the presence of 40 nm polystyrene sphere located 10nm above the ratchet surface. The profiles are taken at a height cutting through the middle of the sphere ($z = 80$ nm) above the substrate. All profiles are plotted using the same colorscale of $\log_{10}(E/E_0) = 0$ to 3. (b) and (c) show z -component of the optical force and potentials experienced by the polystyrene sphere as a function of its position y along the central axis of the ratchet.

Results of simulations for larger nanoparticles

Optical forces and trapping potentials experienced by 200 nm PS spheres and 190 nm PTB7 nanoparticles were calculated using methodology described in section S1.2 of this supplementary document. Material properties used for these simulations/calculations were taken from [S3] and [S4], respectively. For the diameters of the dielectric spheres, 200 nm was used for the PS spheres, as this was the value specified by the manufacturer. For PTB7 nanoparticles, 190 nm was used as the diameter; this value was determined experimentally (see Section 2.2). Results of these calculations are shown in Figure 11.

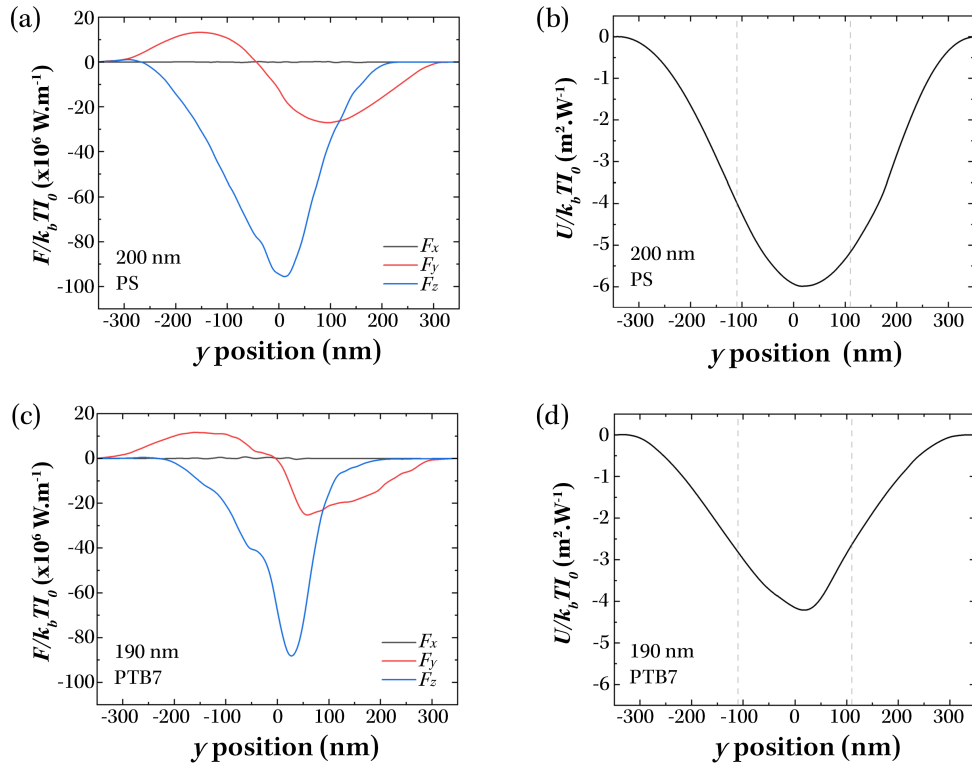


Figure S 11: Numerically-calculated optical forces, (a) and (c), and trapping potentials, (b) and (d), experienced by 200 nm PS and PTB7 nanoparticles above the ratchet structure, respectively. The dashed lines in (b) and (d) denote the top and bottom edges of the ratchet structures, respectively.

Additional ratcheting data

Ratcheting of 200 nm PS spheres

Experimental observation of ratcheting of 200 nm PS spheres and the analysis of results was performed in a manner identical to those for 40 nm PS spheres; the details of these investigations are described in the main text. Figure 12 shows the results for 200 nm PS spheres.

Ratcheting of PTB7 nanoparticles

Fabrication of PTB7 nanoparticles

A colloidal suspension of PTB7 nanoparticles in water, stabilized by pluronic F127 copolymer, were fabricated as follows. Stock PTB7 and F127 solutions were prepared by dissolving 20 mg of PTB7 and 2 g of F127 in 20 mL of THF each. 10 mL of PTB7 stock solution was then mixed with 10 mL of F127 stock solution, and the mixture was added into 100 mL deionised water whilst being sonicated, for 5 minutes. A stirrer bar was added to the solution and the suspension was left stirring for 3 days. The solution was then topped up with deionised water to 100 mL and left for 2 more days to allow THF to evaporate fully.

Determination of mean diameter of PTB7 nanoparticles

The hydrodynamic diameters of PTB7 particles were measured using a ZetaSizer Nano ZS (Malvern Panalytical). For measurements, 2 mL of 5 $\mu\text{g}/\text{mL}$ of PTB7 dispersion was placed into disposable polystyrene cuvettes (DTS0012). Three measurements, with 10 repeats each, were performed at 20°C, with the Malvern software automatically setting the duration of each repeat. Both the correlation curves and the intensity *versus* size curves were indicative of low polydispersity samples (Figure 13). The three measurement results, obtained from cumulative analysis of the correlation curves (performed automatically by Malvern software), were averaged to obtain an average diameter of 203 ± 0.8 nm for PTB7 nanoparticles. Since hydrodynamic radius of nanoparticles is larger than their physical diameter, a somewhat

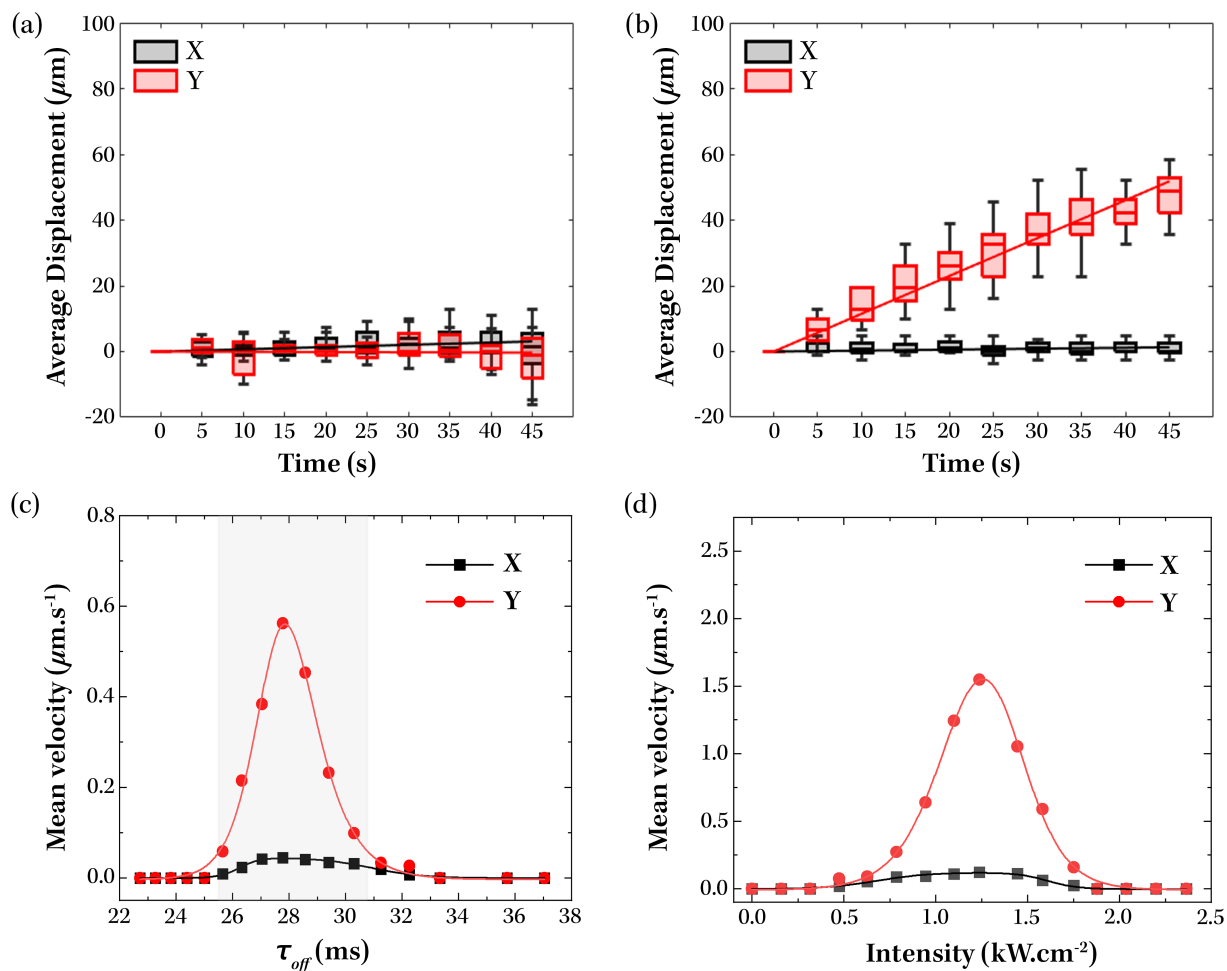


Figure S 12: Experimental results for 200 nm PS spheres. Panels (a) and (b) show the average displacement of detected PS spheres as a function of time, for (a) brownian motion and (b) ratcheting motion, respectively. Motion along the y axis corresponded to motion along the ratcheting axis. Results in (a) were obtained with no external 980 nm illumination, whereas those in (b) were obtained with a chopped 980 nm illumination driving the ratchet. Panels (c) and (d) show the mean velocities of 200 nm PS particles along the x and y directions, recorded under chopped 980 nm illumination of ratchets. In (c), the time that the optical potential remained off (τ_{off}) was varied, with the intensity of 980 nm illumination kept constant at $\sim 0.67 \text{ kW}\cdot\text{cm}^{-2}$. In (d), the intensity of the 980 nm illumination was varied, whilst τ_{off} was kept constant at its optimum value of 27.8 ms. The shaded region in (c) represents the theoretically-predicted range of τ_{off} values where ratchetting should be possible.

smaller size of 190 nm was used in the theoretical calculations of the optimal range of τ_{off} for these conjugated polymer nanospheres.

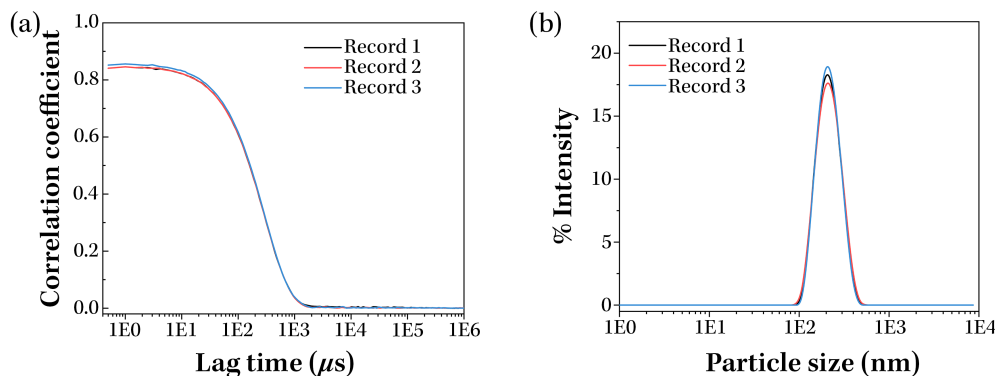


Figure S 13: Dynamic Light Scattering measurements of PTB7 nanoparticles in water. Panel (a) shows correlation curves for the three measurements, and panel (b) shows percent of scattered light as a function of particle size. Each measurement consisted of 10 repeats of duration determined automatically by the ZetaSizer Nano ZS software.

Results of ratcheting for PTB7 nanoparticles

Experimental observation of ratcheting of 190 nm PTB7 nanoparticles and the analysis of results was performed in a manner identical to those for 40 nm PS spheres; the details of these investigations are described in the main text. Figure 14 shows the results for 190 nm PTB7 nanoparticles.

References to Supplementary Information

- [S1] H. Bert, L. Novotny, Principles of Nano-Optics, Cambridge University Press, UK, 2006.
- [S2] D. J. Griffiths, Introduction to Electrodynamics, 4th edition, Cambridge University Press, UK, 2017.
- [S3] N. Sultanova, S. Kasarova, I. Nikolov. Acta Phys. Pol. A **2009**, 116, 585.
- [S4] C. Stelling, C. R. Singh, M. Karg, T. A. F. König, M. Thelakkat, M. Retsch. Sci. Rep. **2017**, 7, 42530.

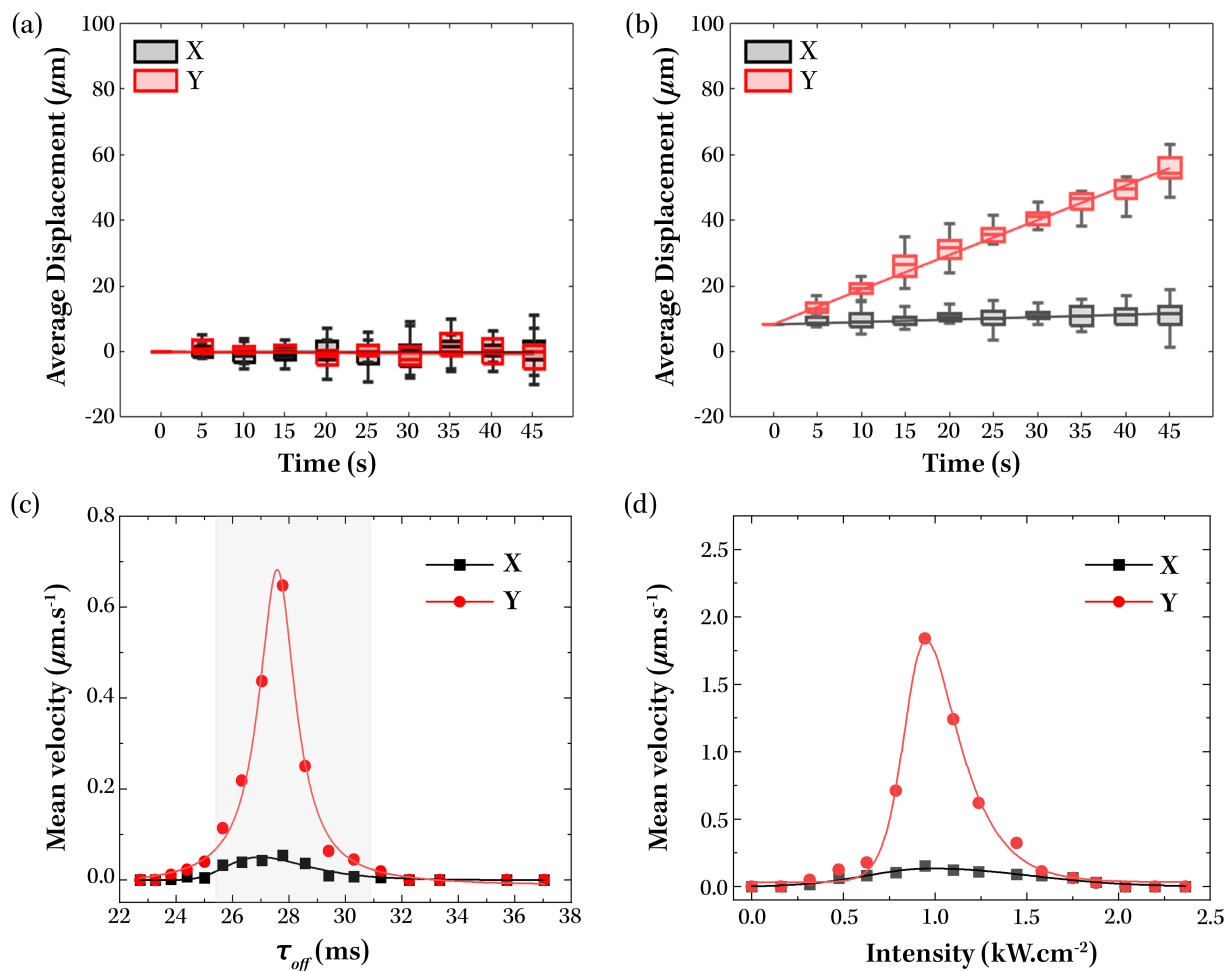


Figure S 14: Experimental results for 190 nm PTB7 spheres. Panels (a) and (b) show the average displacement of detected PTB7 nanoparticles as a function of time, for (a) Brownian motion and (b) ratcheting motion, respectively. Motion along the y axis corresponded to motion along the ratcheting axis. Results in (a) were obtained with no external 980 nm illumination, whereas those in (b) were obtained with a chopped 980 nm illumination driving the ratchet. Panels (c) and (d) show the mean velocities of 190 nm PTB7 nanoparticles along the x and y directions, recorded under chopped 980 nm illumination of ratchets. In (c), the time that the optical potential remained off (τ_{off}) was varied, with the intensity of 980 nm illumination kept constant at $\sim 0.67 \text{ kW}\cdot\text{cm}^{-2}$. In (d), the intensity of the 980 nm illumination was varied, whilst τ_{off} was kept constant at its optimum value of 27.8 ms. The shaded region in (c) represents the theoretically-predicted range of τ_{off} values where ratcheting should be possible.

TOC Graphic

